Geophysical Research Letters

RESEARCH LETTER
10.1029/2024GL108327

On the Tropical Cyclone Integrated Kinetic Energy Balance

A. Avenas[1], A. Mouche[1], J. Knaff[2], X. Carton[1], and B. Chapron[1]

[1]Laboratoire d'Océanographie Physique et Spatiale (LOPS), Ifremer, University Brest, CNRS, IRD, IUEM, Plouzané, France, [2]NOAA/NESDIS Regional and Mesoscale Meteorological Branch, Fort Collins, CO, USA

Key Points:

- High-resolution spaceborne synthetic aperture radar measurements inform on the tropical cyclone kinetic energy balance
- The tropical cyclone integrated kinetic energy balance is controlled by the surface wind decay and thermodynamical characteristics
- Accumulating high-resolution surface wind measurements shall allow to better assess trends in the tropical cyclone destructive potential

Supporting Information:

Supporting Information may be found in the online version of this article.

Correspondence to:

A. Avenas,
arthur.avenas@ifremer.fr

Citation:

Avenas, A., Mouche, A., Knaff, J., Carton, X., & Chapron, B. (2024). On the tropical cyclone integrated kinetic energy balance. *Geophysical Research Letters*, *51*, e2024GL108327. https://doi.org/10.1029/2024GL108327

Received 18 JAN 2024
Accepted 26 JUL 2024

Author Contributions:

Conceptualization: A. Avenas
Formal analysis: A. Avenas
Investigation: A. Avenas
Methodology: A. Avenas
Software: A. Avenas
Supervision: A. Avenas
Validation: A. Avenas
Visualization: A. Avenas
Writing – original draft: A. Avenas, A. Mouche, J. Knaff, X. Carton, B. Chapron
Writing – review & editing: A. Avenas, A. Mouche, J. Knaff, X. Carton, B. Chapron

Abstract Current global historical reanalyzes prevent to adequately examine the role of the near-core surface wind structural properties on tropical cyclones climate trends. Here we provide theoretical and observational evidences that they are crucial for the monitoring of integrated kinetic energy. The kinetic energy balance is reduced to a simple rule involving two parameters characterizing the surface wind structure and directly suggested by the governing equations. The theory is uniquely verified with a database of high-resolution ocean surface winds estimated from all-weather spaceborne synthetic aperture radar. Such measurements provide indirect estimates of a multiplicative constant modulating the kinetic energy balance and associated with the system thermodynamics. Consequently, accumulated high-resolution acquisitions of the ocean surface shall allow to better monitor the integrated kinetic energy and provide new means to tackle climatological studies of tropical cyclones destructiveness.

Plain Language Summary Studying the long-term climate trends of tropical cyclones is challenging because the historical data is not always reliable. One particular issue concerns the accurate reporting of surface wind properties near the core of these storms in past and present records. This study uses both theory and high-resolution surface wind observations from satellite radar to highlight the importance of investigating these properties, specifically for monitoring the total energy, which is a measure of a storm destructive potential. Two spatial scales describing the tropical cyclone wind structure are identified and may be efficiently measured thanks to the high-resolution sensor. The storm energy equilibrium is shown to be controlled by these two spatial scales, in both theory and observations. This equilibrium is also influenced by the temperature characteristics of a storm, which are themselves modulated by environmental and climatological conditions. Consequently, future high-resolution observations from the satellite radar should help better understanding the dependence of integrated kinetic energy with space and time.

1. Introduction

Expressing the combined effect of intensity and size, Integrated Kinetic Energy (IKE) measures the tropical cyclone (TC) destructive potential (Powell & Reinhold, 2007). Understanding the fundamental physics governing this integrated quantity, to better anticipate its evolution in a global warming context, is thus of major importance. Until this day, research studies focused on examining the climate-dependence of intensity (K. Emanuel, 2005; K. Emanuel, 2021; Kossin et al., 2020; Kossin, 2017; Patricola & Wehner, 2018; Sobel et al., 2016; Webster et al., 2005; Wang & Toumi, 2021) and more recently, of size (Chavas & Emanuel, 2010; Knaff et al., 2014; Wang & Toumi, 2021, 2022). Modulated by climate change, the sea surface temperature and the atmospheric temperature and humidity vertical profiles control both TC intensity (Done et al., 2022; Gilford et al., 2017; K. Emanuel, 2007; Wing et al., 2015; Strazzo et al., 2015) and size (Chavas et al., 2016; Lin et al., 2015). While a few methods have been tested to assess past and future IKE trends (Kozar & Misra, 2014; Kreussler et al., 2021; Misra et al., 2013; Morris & Ruf, 2017; Wang & Toumi, 2016, 2021), less is known about how oceanic and atmospheric parameters affect IKE and its variations. This lack of knowledge may be problematic for both operations and research, especially if the TC vitals were to fail capturing parameters that are critical to assess IKE.

In steady-state theories describing axisymmetric TCs, kinetic energy gained through the heat source is hypothesized to balance that lost through the dissipation source (Anthes, 1974; Golitsyn, 2008; K. A. Emanuel, 1986; Kalashnik, 1994; K. A. Emanuel, 1995; Ooyama, 1982; Pearce, 2004; Riehl, 1963). Analytical criteria expressing this steady-state balance may then be derived provided further assumptions on the outflow and inflow layer of TCs. For instance, Riehl (1963) assumes conservation of absolute angular momentum in the upper outflow of TCs. Momentum losses then solely occur in the surface inflow. Without reliable surface wind speed estimates, one way to express momentum losses is to assume potential vorticity (PV) conservation in the inflow, which leads to (Riehl, 1963):

$$C_d r v^2 = \text{cst} \tag{1}$$

With C_d, r and v drag coefficient, radius (*i.e.*, distance from TC center) and tangential velocity, respectively. Under hydrostatic and cyclostrophic balances, the heat source, expressed as the vertical gradient of atmospheric temperature, may be related to the gradient-level wind structure. While the accuracy of Equation 1 in TCs remains to be substantiated, steady-state balance can still be temptingly assessed using surface wind estimates only.

The justification of an overall PV conservation was first facilitated by aircraft data (Riehl, 1963; Riehl & Malkus, 1961) and later by numerical modeling capacities (K. A. Emanuel, 1986; Ooyama, 1982). Observational and experimental research efforts then concentrated on a better characterization of the C_d parameter under high wind speed conditions (Black et al., 2007; Bell et al., 2012; Curcic & Haus, 2020; M. Donelan et al., 2004; Jarosz et al., 2007; M. A. Donelan, 2018; Powell et al., 2003; Soloviev et al., 2014) following Emanuel's steady-state theory (K. A. Emanuel, 1986; K. A. Emanuel, 1995). In such a context, Synthetic Aperture Radar (SAR) has emerged as a promising satellite technology capable of producing fine-scale, wide-swath TC boundary-layer process data in nearly all-weather conditions (A. A. Mouche et al., 2017; A. Mouche et al., 2019). SAR surface wind estimates provide an unprecedented opportunity to examine the TC radial wind structure (Avenas et al., 2023; Combot et al., 2020) and complete existing theories for steady IKE balance.

In the present study, we aim at understanding the fundamental laws governing the steady IKE and its relationship to the TC surface winds. Starting from existing theoretical developments (Charney & Eliassen, 1964; Kalashnik, 1994; Riehl, 1963), we reduce the steady IKE balance to a simple rule that involves two parameters describing the surface wind structure, all measurable with a high-resolution wind profile estimate. This theory is then tested across an extended database of SAR high-resolution observations (178 cases), and discussed with respect to IKE variations estimates from best-track data. The relationship between the SAR-derived surface wind structure parameters and thermodynamic quantities that are most relevant to IKE balance is emphasized. Consequences of Equation 1 on the drag coefficient are also examined through the lens of the SAR measurements. Our investigation suggests that systematic knowledge of the wind structure parameters, especially if they were included in TC vitals, would not only help assessing the IKE balance, but also improve future climatological IKE studies.

2. Preliminary SAR Diagnostic

Spaceborne SAR allows for high spatial resolution estimates of the TC surface wind speeds (see Text S1 in Supporting Information S1). From the 178 SAR surface wind field estimates, Figure 1a displays that of TC Lane on 23 August 2018, while Figure 1b displays that of TC Meranti on 12 September 2016. Both the outer-, near- and inner-core regions of TCs are well captured by SAR observations. The resulting axisymmetric profiles (green curves in Figures 1c and 1d) show that both the axisymmetric maximum intensity ($V_{\max}$) and radius of maximum wind ($R_{\max}$) may be accurately retrieved (Combot et al., 2020). The system center can also be precisely located (Vinour et al., 2021), whose latitude provides the Coriolis parameter (f).

Controlling both the momentum losses and the amplitude of vertical velocities at the top of the boundary layer, the surface wind decay is critical to the IKE balance (see below). It may be quantified in terms of an effective Holland B_s parameter (Holland, 1980), once a Holland parametric wind profile is adjusted (purple curves in Figures 1c and 1d) to the SAR axisymmetric wind profiles estimates (see Text S2 in Supporting Information S1). Note that the wind decay could be characterized using quantities derived from other adjusted parametric wind profiles, for example, the exponent of a modified Rankine vortex. Such alternative quantities are expected to be well correlated to B_s, especially in the near-core region, and thus the results of the present study shall not be affected by this arbitrary choice. Seemingly, Lane and Meranti (Figures 1c and 1d) had substantially different wind decays (hereafter B_s values) while similar TC vitals (*i.e.*, $V_{\max}$ and $R_{\max}$ values). The question arises how this difference impacts the IKE balance.

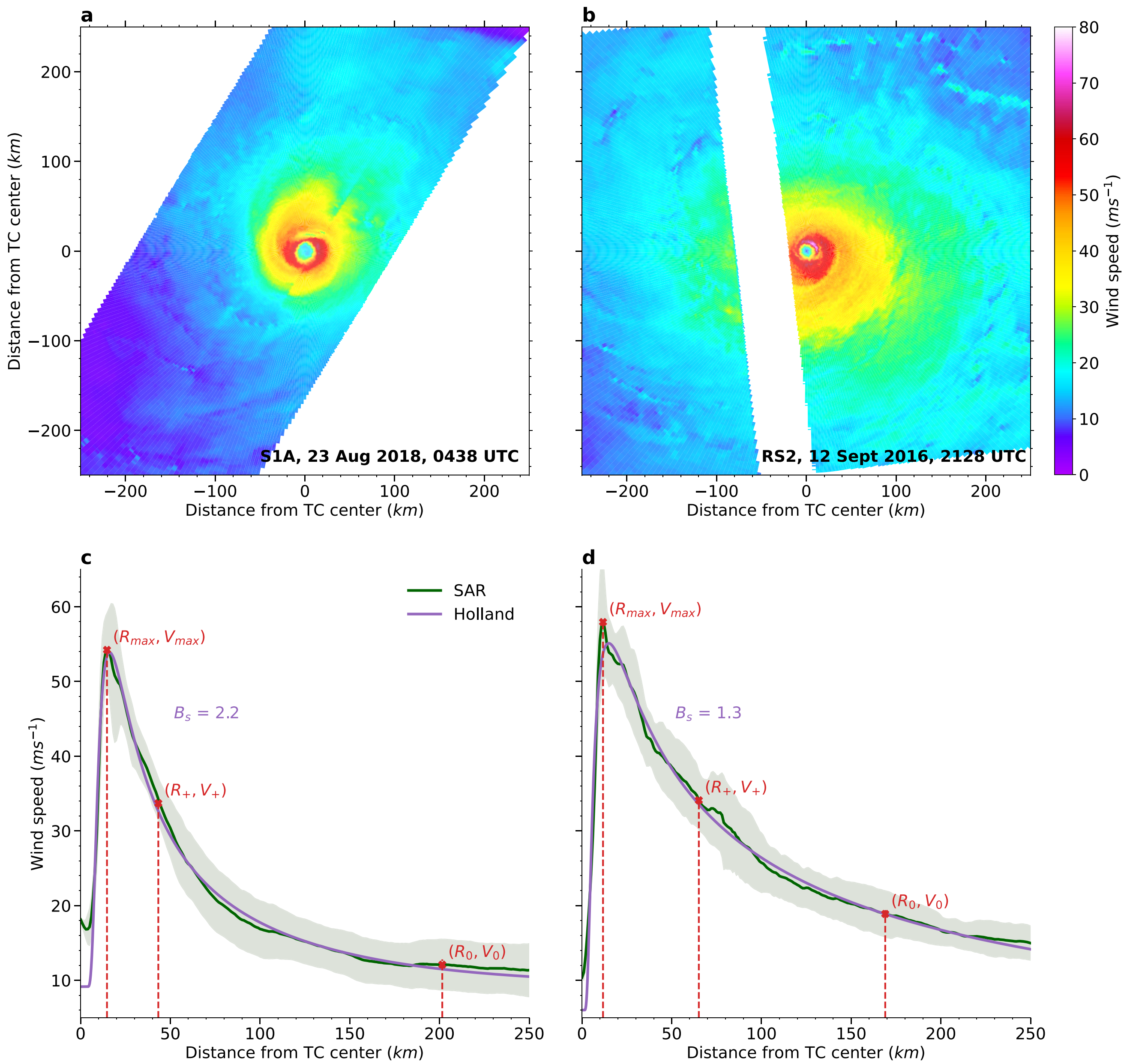

Figure 1. SAR wind speed estimates for (a) Lane and (b) Meranti. Corresponding axisymmetric wind profile (green) and adjusted Holland parametric wind profile (purple) for (c) Lane and (d) Meranti.

3. Deriving the IKE Balance Rule

3.1. Structural Parameters: Definition and Analysis

Assuming a constant air density, the steady-state balance between momentum sink and heat source writes (see Text S3 in Supporting Information S1):

$$\int_0^{R_0} \left[C_d r v^3\right]_{z=0} dr = U_c^2 \left[\frac{C_d r v^2}{\omega_z + f}\right]_{z=0,\ r=R_+} \tag{2}$$

with $\omega_z = \frac{1}{r}\frac{\partial}{\partial r}(rv)$ the vertical component of relative vorticity and U_c a constant which depends on the thermodynamics of the system. Note, $z = 0$ refers to the top of the boundary layer. R_+ and R_0 are two radii characteristic of the IKE balance. The former defines the region of significant upward motions, while the latter defines the integration volume. The amplitude of vertical motions at the top of the boundary layer due to Ekman pumping are expressed by

$$w_E(r) = \frac{1}{r}\frac{d}{dr}\left(\frac{C_d r v^2}{\omega_z + f}\right) \tag{3}$$

Considering a slow numerator variation $C_d r v^2 \approx$ cst, ω_z decreases with r, and w_E becomes close to zero for radii where ω_z is of the same order of the Coriolis parameter f. Conversely, significant upward motions occur in a region where ω_z is at least a few times higher than f. With ω_z monotonically decreasing from a maximum near the TC core to the outermost radii, R_+ may be defined as

$$\omega_z(R_+) = 5f \tag{4}$$

With this definition, the characteristic radius (R_+) and the corresponding surface wind speed (V_+) can be directly estimated using a SAR axisymmetric wind profile (Figures 1c and 1d).

Specifying the integration volume, R_0 is introduced as a natural characteristic radius because of the assumption of absolute angular momentum conservation in the outflow layer (Riehl & Malkus, 1961). Accordingly, if R_0 is defined as the radius where the outflow velocity vanishes, it is directly related to $Ro_{\max} := \frac{V_{\max}}{f R_{\max}}$, the Rossby number evaluated at $R_{\max}$ via

$$\sqrt{2Ro_{\max}} = \frac{R_0}{R_{\max}} \tag{5}$$

This radius (R_0) and the corresponding surface wind speed (V_0) can thus be directly estimated from the SAR surface wind speeds (Figures 1c and 1d).

The two characteristic radii R_0 and R_+ are controlled by the wind structure parameters $Ro_{\max}$ and B_s (see Text S4 in Supporting Information S1). Hence, in what follows we propose to reduce the steady-state balance (*e.g.*, Equation 2) to a relationship involving these structural (B_s and $Ro_{\max}$), in addition to a thermodynamical (U_c) parameter.

3.2. The IKE Balance Rule

Equation 2 involves quantities from the inflow layer, so that recalling the argument of PV conservation (Equation 1), it is tempting to divide each side of Equation 2 by $C_d r v^2$. Equivalently, this corresponds to consider a constant drag coefficient C_d and a relation of the kind $rv^2 \approx$ cst, consistent with the view of K. A. Emanuel (1986) for typical air-sea temperature differences.

Figure 2 shows how the normalized ratio $\kappa_* := \frac{rv^2}{R_+ V_+^2}$ varies as a function of the normalized radius $r_* := \frac{r}{R_+}$ for all the wind profiles of the SAR database. On average (solid black curve), the normalized ratio varies slowly with radius, confirming the approximation $rv^2 =$ cst. Note that these slow radial variations reach a maximum at $r = R_+$. While Equation 4 has been quite arbitrarily, yet reasonably, defined, R_+ appears to correspond to the radius that maximizes, on average, the integrand of the IKE over the SAR database. This local maximum provides information on the radius and area where a TC is the most efficient, that is, where heating is maximum and momentum sink is minimum. This a posteriori justifies our definition for R_+.

For single cases, variations of this normalized ratio κ_* with radius mostly stress the variations in B_s and $Ro_{\max}$. Deviations from the average $\kappa_* \approx 1$ have opposite signs at $R_{\max}$ and R_0. For instance, high B_s and $Ro_{\max}$ values (red profiles covered by the shaded green area) result in $\kappa_*(R_{\max}) > 1$ and $\kappa_*(R_0) < 1$, suggesting that errors inside R_+ compensate those outside R_+ when considering $rv^2 \approx$ cst and simplifying the integral in Equation 2.

Following these results, Equation 2 can be rewritten as

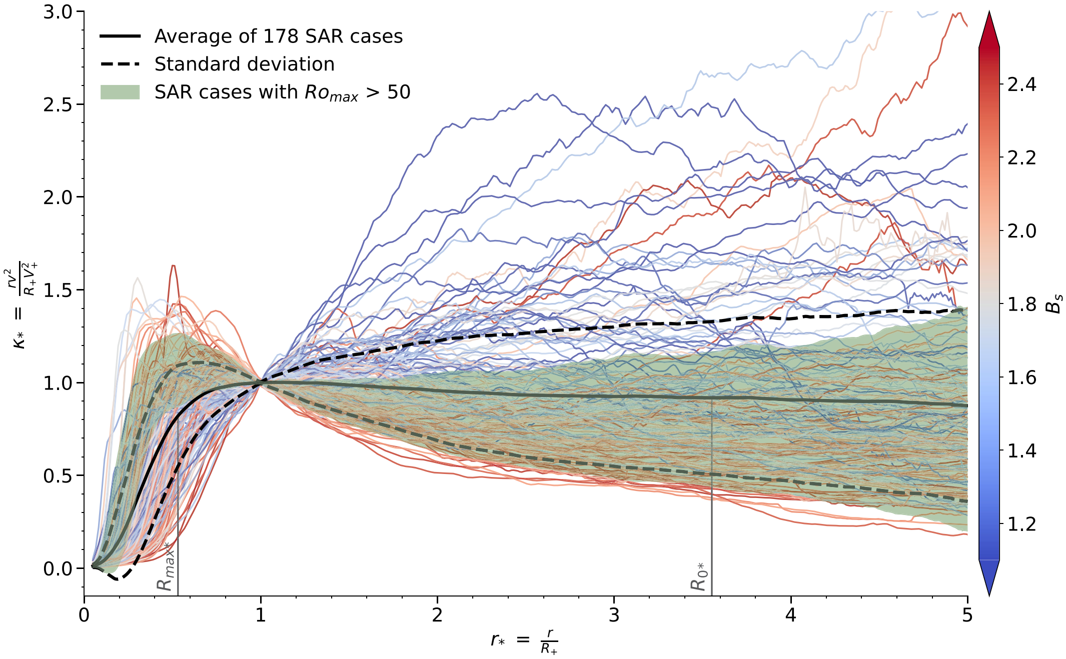

Figure 2. SAR-derived κ_* profiles colored by adjusted Holland B_s parameter (blue to red) and average κ_* profile (black) estimated from the SAR database. Shaded green area denotes the standard deviation interval inside which SAR cases satisfy $Ro_{\max} > 50$.

$$\int_0^{R_0} v(z=0)\, dr = \frac{U_c^2}{6f} \tag{6}$$

Now, the aim is to further express Equation 6 in terms of parameters that can be estimated from SAR data, that is, $V_{\max}$, B_s and $Ro_{\max}$. Here and after it is assumed that the SAR surface wind speed estimates and the corresponding parameters are close to their boundary layer top counterparts. We also recall that, lacking reliable high resolution ocean surface wind vectors data, these parameters were computed using the total wind speed (as provided by SAR) rather than its tangential component. The integral in Equation 6 is approximated as

$$\int_0^{R_0} v(z=0)\, dr \approx \frac{V_{\max} R_0}{2\sqrt{B_s}} \tag{7}$$

Leading to

$$\frac{V_{\max} R_0}{\sqrt{B_s}} \approx \frac{U_c^2}{3f} \tag{8}$$

With use of Equation 5, a TC with steady-state conditions should then obey the following rule:

$$V_{\max}^2 = \frac{U_c^2}{3\sqrt{2}} \sqrt{B_s Ro_{\max}} \tag{9}$$

Which expresses the IKE balance, now reduced to structural parameters (B_s and $Ro_{\max}$) that we can estimate from SAR data. Before testing this rule across the entire SAR database, the degree of IKE steadiness for each observational case must be estimated.

4. Observational Assessment of the IKE Balance Rule

4.1. Best-Track Estimates of IKE Variations

Equation 9 assumes that the TC is in steady-state, that is, that the partial time derivative of azimuthal wind speed and potential temperature can be neglected at each radii. The current spatio-temporal sampling of TC surface observations, including SAR measurements, prevents a direct estimation of the time evolution of these quantities. Yet, neglecting time variations in the potential energy equation, a TC departs from the steady-state assumptions when the absolute temporal variation of IKE is large. Temporal evolution of IKE is given by:

$$\frac{\partial \mathrm{IKE}}{\partial t} = \frac{\partial}{\partial t}\left(\int_0^H \int_0^{R_0} \bar{\rho}_0 r v^2 \, dr \, dz\right) \tag{10}$$

Building on our observational knowledge on the κ_* ratio (Figure 2), the double integral in Equation 10 can be simplified by considering the constant rv^2 at a fixed relevant radius. To evaluate $\frac{\partial IKE}{\partial t}$, we would then need partial time derivative estimates of v and r at this fixed radius. Because of the limited temporal sampling of SAR data, temporal evolutions of these parameters must be evaluated using best-track (Knapp et al., 2010) reanalyzes. However, while $V_{\max}$ best-track uncertainty is rather low (Landsea & Franklin, 2013; Torn & Snyder, 2012), $R_{\max}$ best-track estimates have been shown to be often inconsistent with SAR $R_{\max}$ estimates (Combot et al., 2020). Indeed, $R_{\max}$ is not systematically reanalyzed (unlike $V_{\max}$). From best-track data, the most reliable size parameter is the radius of gale R_{34}, that is, the maximum radial extent of the 34-knots winds (Knaff et al., 2021). Thus, we use the following approximation:

$$\frac{\partial \mathrm{IKE}}{\partial t} \approx \frac{\partial}{\partial t}\left(\int_0^H \bar{\rho}_0 R_{34}^2 V_{34}^2 \, dz\right) \tag{11}$$

where V_{34} is the azimuthal surface wind speed at $r = R_{34}$. Limited by observational capabilities, the dependence of R_{34} in z is unknown. The integral on the vertical component is thus simplified by a multiplication by H. Following the zero PV approximation, we assume that surfaces of constant potential temperature and absolute angular momentum coincide, so that in steady-state H scales as (Shutts, 1981)

$$H = \frac{V_{\max}^2}{g \frac{\Delta\theta}{\theta_0}} \tag{12}$$

where g is standard gravity and $\Delta\theta$ the difference between the potential temperature at the vortex center and its environmental value noted θ_0. Finally, Equation 11 writes

$$\frac{\partial \mathrm{IKE}}{\partial t} = \frac{\bar{\rho}_0 V_{34}^2}{g \frac{\Delta\theta}{\theta_0}} \frac{\partial}{\partial t}\left(V_{\max}^2(t) R_{34}^2(t)\right) \tag{13}$$

where $\bar{\rho}_0 \approx 1.15\ kg.m^{-3}$ and $\frac{\Delta\theta}{\theta_0} \approx 10^{-2}$ are assumed constant in time. Now we may test the IKE balance rule (Equation 9) across the observational database.

4.2. Testing the IKE Balance Rule Across the SAR Database

In Equation 9, we can assume that U_c does not vary too much across different TCs, especially for the present analysis which was restrained to tropical and sub-tropical latitudes (see Text S1 in Supporting Information S1). Figure 3 then shows the SAR observations in a ($V_{\max}^2$, $\sqrt{B_s Ro_{\max}}$) log-linear plane. The corresponding values of absolute partial time derivative of IKE (Equation 13) evaluated using best-track data (see above and Text S5 in Supporting Information S1) are also represented (colors). Cases with the lowest third absolute IKE time derivative estimates (black stars) satisfy the relation of proportionality suggested by Equation 9, as modeled by the least squares regression (dashed black curve, $R^2 = 0.64$), with a variance probably due to both observational errors and variations in the characteristic velocity U_c.

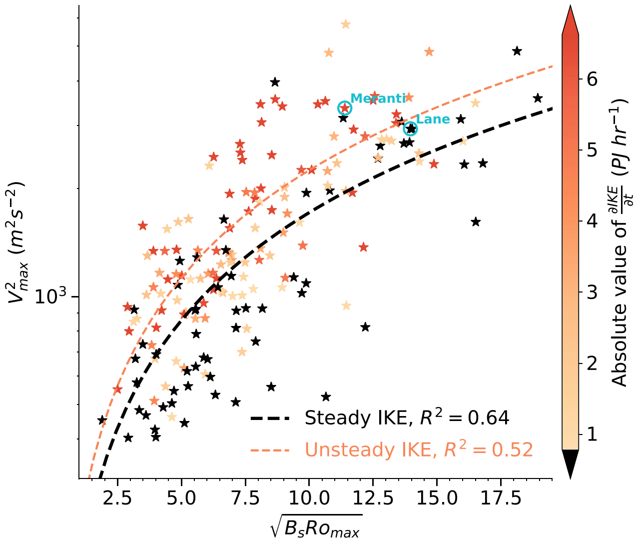

Figure 3. Wind structure parameters estimated from SAR observations (stars) in the plane suggested by Equation 9 (y-axis is in logarithmic scale), and colored by absolute value of $\frac{\partial \mathrm{IKE}}{\partial t}$. Dashed lines denote best-fit linear regressions to cases with the lowest third (black), or highest two thirds (orange/red) absolute IKE time derivative estimates, using a fixed zero intercept.

The velocity U_c characterizes the steady IKE balance in Equation 9. Using known values of thermodynamic constants and assuming that heating occurs in the lowest layers of the TC, we find that $U_c \sim 32$ m/s from its definition (see Text S3 in Supporting Information S1). Based on the steady IKE linear regression slope (black dashed curve in Figure 3), the SAR observations lead to $U_c \sim 27$ m/s, which is close to the theoretical value. We remind readers that this characteristic velocity is that of an average situation. In nature, U_c certainly varies from one TC to another.

Remarkably, cases with the highest two thirds absolute IKE time derivative estimates (orange/red stars) may also be modeled by a least squares regression (dashed orange curve) in the ($V^2_{\max}$, $\sqrt{B_s Ro_{\max}}$) plane, although with more variance ($R^2 = 0.52$) than their steady counterparts, certainly associated with neglected unsteady terms during the derivation of Equation 9. For such cases undergoing significant unsteady IKE transitions, the characteristic velocity $U_c \sim 31$ m/s based on the regression slope is higher than that found for cases with a steady IKE. Here, the steady IKE rule and the resulting characteristic velocity are practical to interpret typical IKE changes across the different groups of cases.

Characterizing the surface winds, the structural parameters (B_s and $Ro_{\max}$) are critical to determine U_c and assess the IKE balance. As an illustration, TC Lane, well captured by a SAR observation (Figures 1a and 1c), had a relatively small IKE variation ($\sim -0.7\ PJhr^{-1}$), corresponding to small changes of $V_{\max}$ and R_{34} in best-track data. In contrast, for TC Meranti (Figures 1b and 1d), the high (positive) temporal variation of IKE ($\sim 24.3\ PJhr^{-1}$) corresponds to a high temporal variation of R_{34} (~ 4.4 kmhr^{-1}) due to an eyewall replacement cycle, while $V_{\max}$ stayed relatively stable (~ 0.3 ms^{-1} hr^{-1}). While Lane and Meranti had similar $Ro_{\max}$ values (90 and 100, respectively) at the time of their acquisitions, their B_s values differed significantly (2.2 and 1.3, respectively), especially considering the typical range of possible B_s values (between 1 and 2.5, see also Avenas et al. (2023)) encountered in the SAR database. Characterizing the effective area where significant energetic exchanges occur, B_s and the corresponding near-core surface wind distribution were recently found to control the short-term evolution of the system (Avenas et al., 2024). Necessary to accurately estimate B_s and $Ro_{\max}$, measurements of the TC wind structure at high-resolution, for instance using SAR sensors, are thus crucial for future IKE studies.

5. Concluding Remarks

Based on existing steady-state theories describing axisymmetric TCs and a PV conservation argument in the inflow, the steady IKE balance was reduced to a simple rule involving two structural parameters suggested by theory and measurable on high-resolution surface data. The derived rule is shown to be consistent with high-resolution SAR observations. In contrast to previous studies (*e.g.*, K. A. Emanuel (1986)), the maximum intensity ($V_{\max}$) that a TC with steady conditions achieves in our work does not involve the exchange coefficients of enthalpy and momentum, whose values at high wind speeds are still actively debated, but rely on an accurate knowledge of the surface winds (B_s and $Ro_{\max}$) and a scalar quantity (U_c). With only one scalar unknown as degree of freedom, the proposed framework thus allows to efficiently assess the TC dynamical state (*i.e.*, both intensity and IKE balance) from the surface winds only.

In Riehl (1963) conceptual framework, the momentum losses are characterized by an assumption of PV conservation close to the surface. Equation 1 was thus considered in the inflow layer and C_d further assumed constant. The SAR database analysis reveals that the distribution of the regions where this assumption is valid depends on the Rossby number $Ro_{\max}$. Indeed, in Figure 2, SAR cases with $Ro_{\max} < 50$ (curves outside the green shaded area) have a κ_* ratio that increases with r, so that if Equation 1 was valid, C_d would decrease with r and thus increase with v, in agreement with the reported literature (M. Donelan et al., 2004; Powell et al., 2003) for wind speeds below hurricane force winds ($\sim$33 m/s). At higher Rossby numbers $Ro_{\max} > 50$ (curves inside the green shaded area), the decrease of κ_* with r between R_+ and $R_{\max}$ suggests that C_d decreases/saturates. For such TCs, hurricane force winds are largely exceeded in this area and the suggested decrease/saturation of C_d agrees with reported estimates under hurricane conditions (Black et al., 2007; Bell et al., 2012; Curcic & Haus, 2020; M. Donelan et al., 2004; Jarosz et al., 2007; M. A. Donelan, 2018; Powell et al., 2003; Soloviev et al., 2014). At radii greater than R_+, the assumption expressed by Equation 1 certainly breaks down because the κ_* ratio decreases with r. A relation of relative angular momentum conservation $rv \approx$ cst is approached, so that friction is presumably small in this region. As a result, vertical velocities at the top of the boundary layer are close to zero, because both $C_d rv^2$ and ω_z are small in Equation 3. Further understanding how R_+, or more generally the wind decay, is related to C_d increase/decrease with wind speed is beyond the scope of this study, but SAR observations may be instrumental to help better determining the spatial distribution of C_d.

Assuming steady conditions for the system, Equation 9 can be used to indirectly estimate the characteristic velocity U_c from a given SAR observation. Strongly influencing the IKE balance (Equation 9), U_c depends on both oceanic and atmospheric parameters. As a consequence, our understanding of the basin- and climate-dependence of U_c, and in turn the IKE, should benefit from the increasing number of spaceborne SAR sensors (*e.g.*, the recently launched Radarsat Constellation Mission) and the corresponding accumulation of U_c estimates. In the absence of SAR, the developed theory suggests that the knowledge of the near-core wind decay for example, with B_s and the maximum Rossby number with $Ro_{\max}$ (or equivalently R_0 and R_+), along with the maximum intensity $V_{\max}$, should be sufficient to estimate the TC characteristic velocity U_c and assess the IKE balance. Presently, while the maximum intensity may be one of the most reliable parameters in the TC vitals, accurate estimates of the near-core wind decay and the maximum Rossby number are not systematically available. Consistently including reliable estimates of these two structural parameters in operational and historical records would allow, in combination with theory, to better monitor short- and long-term changes in TCs destructive potential.

Data Availability Statement

Data sets for this research are freely available online at https://cyclobs.ifremer.fr/app/tropical using the steps described at https://cyclobs.ifremer.fr/app/docs/.

Acknowledgments

This work was financially supported by the ERC Synergy project 856408-STUOD. The SAR database was obtained from IFREMER/CyclObs and produced with the SAR wind processor co-developed by IFREMER and CLS. J. Knaff thanks NOAA/Center for Satellite Applications and Research for providing the time work on this subject. The views, opinions, and findings contained in this report are those of the authors and should not be construed as an official National Oceanic and Atmospheric Administration or U.S. government position, policy, or decision. We also acknowledge an anonymous reviewer for helpful comments.

References

Anthes, R. A. (1974). The dynamics and energetics of mature tropical cyclones. *Reviews of Geophysics*, *12*(3), 495–522. https://doi.org/10.1029/rg012i003p00495

Avenas, A., Chapron, B., Mouche, A., Platzer, P., & Vinour, L. (2024). Revealing short-term dynamics of tropical cyclone wind speeds from satellite synthetic aperture radar. *Scientific Reports*, *14*(1), 12808. https://doi.org/10.1038/s41598-024-61384-w

Avenas, A., Mouche, A., Tandeo, P., Piolle, J.-F., Chavas, D., Fablet, R., et al. (2023). Reexamining the estimation of tropical cyclones radius of maximum wind from outer size with an extensive synthetic aperture radar dataset. *Monthly Weather Review*, *151*(12), 3169–3189. https://doi.org/10.1175/mwr-d-23-0119.1

Bell, M. M., Montgomery, M. T., & Emanuel, K. A. (2012). Air–sea enthalpy and momentum exchange at major hurricane wind speeds observed during cblast. *Journal of the Atmospheric Sciences*, *69*(11), 3197–3222. https://doi.org/10.1175/jas-d-11-0276.1

Black, P. G., D'Asaro, E. A., Drennan, W. M., French, J. R., Niiler, P. P., Sanford, T. B., et al. (2007). Air–sea exchange in hurricanes: Synthesis of observations from the coupled boundary layer air–sea transfer experiment. *Bulletin of the American Meteorological Society*, *88*(3), 357–374. https://doi.org/10.1175/bams-88-3-357

Charney, J. G., & Eliassen, A. (1964). On the growth of the hurricane depression. *Journal of the Atmospheric Sciences*, *21*(1), 68–75. https://doi.org/10.1175/1520-0469(1964)021<0068:otgoth>2.0.co;2

Chavas, D. R., & Emanuel, K. A. (2010). A quikscat climatology of tropical cyclone size. *Geophysical Research Letters*, *37*(18). https://doi.org/10.1029/2010gl044558

Chavas, D. R., Lin, N., Dong, W., & Lin, Y. (2016). Observed tropical cyclone size revisited. *Journal of Climate*, *29*(8), 2923–2939. https://doi.org/10.1175/jcli-d-15-0731.1

Combot, C., Mouche, A., Knaff, J., Zhao, Y., Zhao, Y., Vinour, L., et al. (2020). Extensive high-resolution synthetic aperture radar (sar) data analysis of tropical cyclones: Comparisons with sfmr flights and best track. *Monthly Weather Review*, *148*(11), 4545–4563. https://doi.org/10.1175/mwr-d-20-0005.1

Curcic, M., & Haus, B. K. (2020). Revised estimates of ocean surface drag in strong winds. *Geophysical Research Letters*, *47*(10), e2020GL087647. https://doi.org/10.1029/2020gl087647

Done, J. M., Lackmann, G. M., & Prein, A. F. (2022). The response of tropical cyclone intensity to changes in environmental temperature. *Weather and Climate Dynamics*, *3*(2), 693–711. https://doi.org/10.5194/wcd-3-693-2022

Donelan, M., Haus, B. K., Reul, N., Plant, W., Stiassnie, M., Graber, H., et al. (2004). On the limiting aerodynamic roughness of the ocean in very strong winds. *Geophysical Research Letters*, *31*(18). https://doi.org/10.1029/2004gl019460

Donelan, M. A. (2018). On the decrease of the oceanic drag coefficient in high winds. *Journal of Geophysical Research: Oceans*, *123*(2), 1485–1501. https://doi.org/10.1002/2017jc013394

Emanuel, K. (2005). Increasing destructiveness of tropical cyclones over the past 30 years. *Nature*, *436*(7051), 686–688. https://doi.org/10.1038/nature03906

Emanuel, K. (2007). Environmental factors affecting tropical cyclone power dissipation. *Journal of Climate*, *20*(22), 5497–5509. https://doi.org/10.1175/2007jcli1571.1

Emanuel, K. (2021). Atlantic tropical cyclones downscaled from climate reanalyses show increasing activity over past 150 years. *Nature Communications*, *12*(1), 7027. https://doi.org/10.1038/s41467-021-27364-8

Emanuel, K. A. (1986). An air-sea interaction theory for tropical cyclones. part i: Steady-state maintenance. *Journal of the Atmospheric Sciences*, *43*(6), 585–605. https://doi.org/10.1175/1520-0469(1986)043<0585:aasitf>2.0.co;2

Emanuel, K. A. (1995). Sensitivity of tropical cyclones to surface exchange coefficients and a revised steady-state model incorporating eye dynamics. *Journal of the Atmospheric Sciences*, *52*(22), 3969–3976. https://doi.org/10.1175/1520-0469(1995)052<3969:sotcts>2.0.co;2

Gilford, D. M., Solomon, S., & Emanuel, K. A. (2017). On the seasonal cycles of tropical cyclone potential intensity. *Journal of Climate*, *30*(16), 6085–6096. https://doi.org/10.1175/jcli-d-16-0827.1

Golitsyn, G. (2008). Polar lows and tropical hurricanes: Their energy and sizes and a quantitative criterion for their generation. *Izvestiya - Atmospheric and Oceanic Physics*, *44*(5), 537–547. https://doi.org/10.1134/s0001433808050010

Holland, G. J. (1980). An analytic model of the wind and pressure profiles in hurricanes. *Monthly Weather Review*, *108*(8), 1212–1218. https://doi.org/10.1175/1520-0493(1980)108<1212:aamotw>2.0.co;2

Jarosz, E., Mitchell, D. A., Wang, D. W., & Teague, W. J. (2007). Bottom-up determination of air-sea momentum exchange under a major tropical cyclone. *Science*, *315*(5819), 1707–1709. https://doi.org/10.1126/science.1136466

Kalashnik, M. (1994). On the maximum wind velocity in the tropical cyclone. Izvestiâ Akademii nauk SSSR. *Fizika Atmosfery i Okeana*, *30*(1), 26–30.

Knaff, J. A., Longmore, S. P., & Molenar, D. A. (2014). An objective satellite-based tropical cyclone size climatology. *Journal of Climate*, *27*(1), 455–476. https://doi.org/10.1175/jcli-d-13-00096.1

Knaff, J. A., Sampson, C. R., Kucas, M. E., Slocum, C. J., Brennan, M. J., Meissner, T., et al. (2021). Estimating tropical cyclone surface winds: Current status, emerging technologies, historical evolution, and a look to the future. *Tropical Cyclone Research and Review*, *10*(3), 125–150. https://doi.org/10.1016/j.tcrr.2021.09.002

Knapp, K. R., Kruk, M. C., Levinson, D. H., Diamond, H. J., & Neumann, C. J. (2010). The international best track archive for climate stewardship (ibtracs) unifying tropical cyclone data. *Bulletin of the American Meteorological Society*, *91*(3), 363–376. https://doi.org/10.1175/2009bams2755.1

Kossin, J. P. (2017). Hurricane intensification along United States coast suppressed during active hurricane periods. *Nature*, *541*(7637), 390–393. https://doi.org/10.1038/nature20783

Kossin, J. P., Knapp, K. R., Olander, T. L., & Velden, C. S. (2020). Global increase in major tropical cyclone exceedance probability over the past four decades. *Proceedings of the National Academy of Sciences*, *117*(22), 11975–11980. https://doi.org/10.1073/pnas.1920849117

Kozar, M. E., & Misra, V. (2014). Statistical prediction of integrated kinetic energy in north atlantic tropical cyclones. *Monthly Weather Review*, *142*(12), 4646–4657. https://doi.org/10.1175/mwr-d-14-00117.1

Kreussler, P., Caron, L.-P., Wild, S., Loosveldt Tomas, S., Chauvin, F., Moine, M.-P., et al. (2021). Tropical cyclone integrated kinetic energy in an ensemble of highresmip simulations. *Geophysical Research Letters*, *48*(5), e2020GL090963. https://doi.org/10.1029/2020gl090963

Landsea, C. W., & Franklin, J. L. (2013). Atlantic hurricane database uncertainty and presentation of a new database format. *Monthly Weather Review*, *141*(10), 3576–3592. https://doi.org/10.1175/mwr-d-12-00254.1

Lin, Y., Zhao, M., & Zhang, M. (2015). Tropical cyclone rainfall area controlled by relative sea surface temperature. *Nature Communications*, *6*(1), 6591. https://doi.org/10.1038/ncomms7591

Misra, V., DiNapoli, S., & Powell, M. (2013). The track integrated kinetic energy of atlantic tropical cyclones. *Monthly Weather Review*, *141*(7), 2383–2389. https://doi.org/10.1175/mwr-d-12-00349.1

Morris, M., & Ruf, C. S. (2017). Estimating tropical cyclone integrated kinetic energy with the cygnss satellite constellation. *Journal of Applied Meteorology and Climatology*, *56*(1), 235–245. https://doi.org/10.1175/jamc-d-16-0176.1

Mouche, A., Chapron, B., Knaff, J., Zhao, Y., Zhang, B., & Combot, C. (2019). Copolarized and cross-polarized sar measurements for high-resolution description of major hurricane wind structures: Application to irma category 5 hurricane. *Journal of Geophysical Research: Oceans*, *124*(6), 3905–3922. https://doi.org/10.1029/2019jc015056

Mouche, A. A., Chapron, B., Zhang, B., & Husson, R. (2017). Combined co-and cross-polarized sar measurements under extreme wind conditions. *IEEE Transactions on Geoscience and Remote Sensing*, *55*(12), 6746–6755. https://doi.org/10.1109/tgrs.2017.2732508

Ooyama, K. V. (1982). Conceptual evolution of the theory and modeling of the tropical cyclone. *Journal of the Meteorological Society of Japan. Ser. II*, *60*(1), 369–380. https://doi.org/10.2151/jmsj1965.60.1_369

Patricola, C. M., & Wehner, M. F. (2018). Anthropogenic influences on major tropical cyclone events. *Nature*, *563*(7731), 339–346. https://doi.org/10.1038/s41586-018-0673-2

Pearce, R. P. (2004). An axisymmetric model of a mature tropical cyclone incorporating azimuthal vorticity. *Quarterly Journal of the Royal Meteorological Society*, *130*(596), 259–293. https://doi.org/10.1256/qj.02.86

Powell, M. D., & Reinhold, T. A. (2007). Tropical cyclone destructive potential by integrated kinetic energy. *Bulletin of the American Meteorological Society*, *88*(4), 513–526. https://doi.org/10.1175/bams-88-4-513

Powell, M. D., Vickery, P. J., & Reinhold, T. A. (2003). Reduced drag coefficient for high wind speeds in tropical cyclones. *Nature*, *422*(6929), 279–283. https://doi.org/10.1038/nature01481

Riehl, H. (1963). Some relations between wind and thermal structure of steady state hurricanes. *Journal of the Atmospheric Sciences*, *20*(4), 276–287. https://doi.org/10.1175/1520-0469(1963)020<0276:srbwat>2.0.co;2

Riehl, H., & Malkus, J. (1961). Some aspects of hurricane daisy, 1958. *Tellus*, *13*(2), 181–213. https://doi.org/10.3402/tellusa.v13i2.9495

Shutts, G. (1981). Hurricane structure and the zero potential vorticity approximation. *Monthly Weather Review*, *109*(2), 324–329. https://doi.org/10.1175/1520-0493(1981)109<0324:hsatzp>2.0.co;2

Sobel, A. H., Camargo, S. J., Hall, T. M., Lee, C.-Y., Tippett, M. K., & Wing, A. A. (2016). Human influence on tropical cyclone intensity. *Science*, *353*(6296), 242–246. https://doi.org/10.1126/science.aaf6574

Soloviev, A. V., Lukas, R., Donelan, M. A., Haus, B. K., & Ginis, I. (2014). The air-sea interface and surface stress under tropical cyclones. *Scientific Reports*, *4*(1), 5306. https://doi.org/10.1038/srep05306

Strazzo, S., Elsner, J. B., & LaRow, T. (2015). Quantifying the sensitivity of maximum, limiting, and potential tropical cyclone intensity to sst: Observations versus the fsu/coaps global climate model. *Journal of Advances in Modeling Earth Systems*, *7*(2), 586–599. https://doi.org/10.1002/2015ms000432

Torn, R. D., & Snyder, C. (2012). Uncertainty of tropical cyclone best-track information. *Weather and Forecasting*, *27*(3), 715–729. https://doi.org/10.1175/waf-d-11-00085.1

Vinour, L., Jullien, S., Mouche, A., Combot, C., & Mangeas, M. (2021). Observations of tropical cyclone inner-core fine-scale structure, and its link to intensity variations. *Journal of the Atmospheric Sciences*, *78*(11), 3651–3671. https://doi.org/10.1175/jas-d-20-0245.1

Wang, S., & Toumi, R. (2016). On the relationship between hurricane cost and the integrated wind profile. *Environmental Research Letters*, *11*(11), 114005. https://doi.org/10.1088/1748-9326/11/11/114005

Wang, S., & Toumi, R. (2021). Recent tropical cyclone changes inferred from ocean surface temperature cold wakes. *Scientific Reports*, *11*(1), 22269. https://doi.org/10.1038/s41598-021-01612-9

Wang, S., & Toumi, R. (2022). An analytic model of the tropical cyclone outer size. *NPJ Climate and Atmospheric Science*, *5*(1), 46. https://doi.org/10.1038/s41612-022-00270-6

Webster, P. J., Holland, G. J., Curry, J. A., & Chang, H.-R. (2005). Changes in tropical cyclone number, duration, and intensity in a warming environment. *Science*, *309*(5742), 1844–1846. https://doi.org/10.1126/science.1116448

Wing, A. A., Emanuel, K., & Solomon, S. (2015). On the factors affecting trends and variability in tropical cyclone potential intensity. *Geophysical Research Letters*, *42*(20), 8669–8677. https://doi.org/10.1002/2015gl066145